Journal of Geophysical Research: Oceans

Supporting Information for

Bioturbation and the δ^{56}Fe Signature of Dissolved Iron Fluxes from Marine Sediments

Sebastiaan J. van de Velde[1,2], Andrew W. Dale[3], and Sandra Arndt[1]

[1] Department of Geoscience, Environment & Society, Université Libre de Bruxelles, Brussels, Belgium
[2] Operational Directorate Natural Environment, Royal Belgian Institute of Natural Sciences, Brussels, Belgium
[3] GEOMAR Helmholtz Centre for Ocean Research Kiel, Kiel, Germany

Contents of this file

Introduction

Extended description of the diagenetic model set-up, reaction set and parametrization.

Text S1. Early diagenetic model used for calibration of iron isotope fractionations ('site-specific model')

Our first goal was to calibrate the iron isotope fractionations that are induced during sedimentary iron cycling. To this end, we constructed an early diagenetic model and calibrated it on two sites where iron isotopes of pore-water and solid-phase fractions were measured (see main text; Severmann et al., 2006). Because our focus was on the concentrations and isotope values measured by Severmann et al. (2006), we decided to omit any elements for which we had no data, as to avoid over-parameterisation of our model. Hence, we did not include nitrogen or manganese and omitted moderately reactive, poorly reactive and unreactive iron mineral classes. We did however make a subdivision in the highly reactive class to contain 'fresh' iron oxides and 'aged' iron oxides, as is commonly done (Berg et al., 2003; van de Velde et al., 2020). We also omitted elemental sulphur or hydrogen.

S1.1 Diagenetic model formulation

The early diagenetic model follows the standard approach to describe reaction-transport in marine sediment (Wang and Van Cappellen, 1996; Boudreau, 1997; Berg et al., 2003; Meysman et al., 2003). The core of this reaction-transport model consists of a set of mass balance equations of the advection-diffusion-reaction form (Boudreau, 1997; Meysman et al., 2005). Adopting the assumption of steady-state compaction, the balance equation for a pore-water solute and solid components becomes (Meysman et al., 2005):

$$\begin{aligned} \phi_F \frac{\partial C_{D,i}}{\partial t} &= \frac{\partial}{\partial z}\left[\phi_F D_i \frac{\partial C_{D,i}}{\partial z} - \phi_F v_F C_{D,i} \right] + \phi_F \alpha_i \left(C_{D,i}^{OW} - C_{D,i} \right) + \sum_k \nu_{i,k} R_k \\ (1-\phi_F) \frac{\partial C_{S,i}}{\partial t} &= \frac{\partial}{\partial z}\left[(1-\phi_F) D_B \frac{\partial C_{S,i}}{\partial z} - (1-\phi_F) v_S C_{S,i} \right] + \sum_k \nu_{i,k} R_k \end{aligned} \quad [1]$$

The quantity $C_{D,i}$ represents the concentration of a pore-water compound, $C_{D,i}^{OW}$ is the value in the overlying water, ϕ_F denotes the porosity (implemented via an exponentially decreasing depth relation as described below), ϕ_F^{∞} is the asymptotic porosity at depth, D_i is the diffusion coefficient, v_F is the burial velocity of the pore fluids, v_S is the burial velocity of the solids, and z is the depth into the sediment. The concentration $C_{S,i}$ of a solid compound is expressed per unit volume of solid sediment. The quantities R_k represent the rates of the biogeochemical reactions (expressed per bulk sediment volume), where $\nu_{i,k}$ is the stoichiometric coefficient of the *i*-th species in the *k*-th reaction. The effect of bioturbation (bio-mixing and bio-irrigation) is implemented by the bio-mixing parameter D_B and the bio-irrigation parameter α_i, which is solute specific (Meile et al., 2005).

The model includes a set of transport processes that is characteristic for cohesive (i.e. low permeable) sediments impacted by fauna: (1) solute diffusion in the pore water, (2)

downward advection due to sediment accumulation, (3) bio-mixing and (4) bio-irrigation. Pore water advection induced by bottom currents and waves, characteristic for permeable sediments, is not incorporated. The solute flux due to molecular diffusion and advection is described by Fick's first law (Fick, 1855),

$$J_D = -\phi D_i \frac{\partial C_{D,i}}{\partial z} + \phi v C_{D,i} \quad [2]$$

where the molecular diffusion coefficient D_i^{mol} is first calculated as a function of temperature and salinity using the CRAN:marelac package (Soetaert et al., 2010a) and corrected for tortuosity according to the modified Wiessberg relation of Boudreau (1996), $D_i = D_i^{mol} / (1 - 2\ln \phi_F)$.

S1.1.1 Model parameterisation: porosity and transport processes

An exponential declining porosity profile was imposed,

$$\phi_F = \phi_F^0 + (\phi_F^0 - \phi_F^\infty) e^{-z/z_{att}} \quad [3]$$

where φ_F^0 is 0.948, φ_F^∞ is 0.824 and z_{att} is 3.6 cm for the model calibration. This is the porosity profile used by Meysman et al. (2003), when they modelled the Santa Barbara site (Figure S1a). A change in porosity implies sediment compaction with depth, and different burial velocities for solutes and solids. The model adopts a constant sedimentation velocity in consolidated sediment of $v_S = v_F = 0.25$ cm yr^{-1}, which is the sedimentation velocity of both sites that were used to calibrate the model parameters (Severmann et al., 2006). The depth-dependent advection velocities were calculated from the porosity profile and the burial velocities in consolidated sediment using the CRAN:ReacTran package (Soetaert and Meysman, 2012).

The presence of bioturbation is modelled as two different extra transport parameters; bio-mixing and bio-irrigation. Following the conventional description, bio-mixing is modelled as a diffusive-like process (Boudreau, 1997; Meysman et al., 2010)

$$J_b = -(1-\phi_F) D_b \frac{\partial C_{S,i}}{\partial z} \quad [4]$$

Benthic fauna require food resources (organic matter) that arrive from the overlying water at the top of the sediment pile, and thus most of their activity occurs near the sediment-water interface, and decreases with depth (Boudreau, 1998). The bio-diffusivity coefficient accordingly follows a sigmoidal depth profile

$$D_b(z) = D_{b,0} \exp\left(-\frac{(z - z_L)}{0.25 z_{bm}}\right) \Big/ \left(1 + \exp\left(-\frac{(z - z_L)}{0.25 z_{bm}}\right)\right) \quad [5]$$

where $D_{b,0}$ is the bio-diffusivity at the sediment-water interface, z_L is the depth of the mixed layer and z_{bm} is an attenuation coefficient determining the transition zone from mixed to unmixed sediment horizons. Bio-mixing is governed by two separate parameters: the intensity of mixing as represented by the bio-diffusivity, $D_{b,0}$, and the depth of the mixed layer, as represented by z_L (the width of the transition zone z_{bm} is of secondary

importance) (Figure S1b). In natural systems, these two parameters are correlated (Boudreau, 1998; Middelburg, 2019). Hence, to account for this interdependency, and facilitate model sensitivity analysis, the mixing depth was made dependent on the bio-diffusivity by means of the following relation (van de Velde and Meysman, 2016),

$$z_L = z_{L,0} + z_{L,\max}\left(1 - e^{-D_{b,0}/D_{b,ref}}\right) \quad [6]$$

where $z_{L,0}$ (=1 cm) is the minimum depth of bioturbation, $z_{L,\max}$ is the maximum mixing depth ($z_{L,0}$ + $z_{L,\max}$ = 10 cm; Boudreau, 1998) and $D_{b,ref}$ (=3 $cm^2\ yr^{-1}$) is a reference mixing intensity (Figure S1d; van de Velde and Meysman, 2016). This relation implies that the mixing depth first rapidly increases with a rising mixing intensity, but then saturates. This saturation response implies that when the population density of the infauna increases, the burrowing depth does not necessarily increase.

The second effect of bioturbating fauna, bio-irrigation, is typically described as a non-local exchange process, in which pore water parcels are exchanged with bottom water parcels (Boudreau, 1984)

$$I_{irr}(z) = \alpha(z)(C_{D,i}^{ow} - C_{D,i}(z)) \quad [7]$$

where the quantity $\alpha(z)$ represents the depth-dependent irrigation intensity, $C_{D,i}^{ow}$ is the solute concentration of the bottom water, and $C_{D,i}(z)$ is the solute concentration at depth z. The bio-irrigation effect is generally most pronounced in the top layer of the sediment. However, the faunal activities that induce bio-mixing (e.g. locomotion and burrow construction) are different from those that underlie bio-irrigation (e.g. burrow ventilation), and so the depth dependency of both processes must not be the same. Indeed, in natural systems, bio-irrigation is best represented using an exponential relation of the form (Kristensen et al., 2018)

$$\alpha(z) = \alpha_0 e^{-z/z_{irr}} \quad [8]$$

where α_0 is the bio-irrigation coefficient at the sediment-water interface and z_{irr} is an attenuation coefficient determining the transition zone from irrigated to un-irrigated sediment horizons (Figure S1c). The z_{irr} parameter is adapted for each simulation to so that depth of bio-irrigation matches the depth of bio-mixing. Following Meile et al. (2005), we introduce solute-specific irrigation coefficients, to capture the differential biogeochemical behaviour of individual pore-water species (specifically reduced Fe^{2+} and ΣH_2S). The fast oxidation kinetics of Fe^{2+} and ΣH_2S means that these species are generally not flushed out of the sediment, but are oxidised in the worm burrow. During model calibration, we fitted the solute specific irrigation coefficients to be $\alpha_{\Sigma H_2S} = 0.5\alpha$ and $\alpha_{Fe^{2+}} = 0.05\alpha$.

S1.1.2 Model parameterisation: biogeochemical reaction set

The focus of this reaction-transport model was to calibrate the iron isotope fractionation factors. Therefore, we tailored the reaction set to the available data of the two field sites presented in Severmann et al. (2006). The dataset only contained information about highly

reactive iron minerals (reactive iron oxides, iron sulphides, sorbed iron and pyrite). Therefore, we omitted moderately reactive, poorly reactive and unreactive iron mineral classes, and made a subdivision in the highly reactive class to contain 'fresh' iron oxides (comparable to 2-line ferrihydrite; Poulton et al., 2004; van de Velde and Meysman, 2016) and 'aged' iron oxides (comparable to goethite; Poulton et al., 2004). Additionally, to keep the reaction set as simple as possible, we did not include elemental sulphur or hydrogen, but instead allowed pyrite precipitation after reaction of FeS with sulphide and sulphate (see, e.g., van de Velde et al., 2020). The reactions included in the model are listed in Table S1, the reaction equations are listed in Table S2 and the parameters and boundary conditions are given in Table S3.

Table S1 specifies the 16 reactions that are included in the reaction list. The model incorporates a detailed description of Fe cycling, including dissimilatory iron reduction, adsorption of Fe^{2+} on solid phase particles, aerobic oxidation of dissolved and adsorbed Fe^{2+}, multiple iron oxides fractions with different kinetics towards sulphide, iron oxide aging, formation and dissolution of iron sulphide, and pyrite precipitation. Additionally, we include a realistic description of organic matter degradation kinetics by approximating the reactive continuum model (Boudreau and Ruddick, 1991) by a 14 component multi-G model (Dale et al., 2015). Each of the organic matter ('G') fractions can be degraded by four different mineralisation pathways; aerobic respiration (AR), dissimilatory iron reduction (DIR), sulphate reduction (SR) and methanogenesis (MG) (Table S1, note that these redox pathways are implemented for each of the organic matter fractions). The redox sequence is implemented via conventional limitation-inhibition formulations (Table S2) (Soetaert et al., 1996).

Iron oxides are modelled as two separate fractions; fresh iron oxides and aged iron oxides, where the fresh iron oxide fraction can reduce organic matter and oxidise sulphide, and the aged iron oxides only reacts with sulphide (Berg et al., 2003). The reactivity of these two fractions towards sulphide broadly corresponds to the reactivity lepidocrocite ('fresh') and goethite ('aged'), as determined by Poulton et al. (2004). Organic matter mineralisation coupled to iron oxide reduction released ferrous iron (Fe^{2+}) in the pore water, which can adsorb on solid-phase particles, which is implemented as a thermodynamic equilibrium

$$\left[X \equiv Fe^{2+} \right] = K_{ads}^{Fe^{2+}} \left[Fe^{2+} \right] \quad [9]$$

where $K_{ads}^{Fe^{2+}}$ is the dimensionless adsorption constant. Both dissolved and adsorbed forms can become re-oxidised by oxygen, or ferrous iron precipitate as iron sulphide (Table S1). Sulphate reduction produces free sulphide, which can be re-oxidised by oxygen, re-oxidised by iron oxides, precipitated as FeS, reacted with FeS to form FeS_2 (Table S1). When electron acceptors (O_2, FeOOH, SO_4^{2-}) are depleted, methanogenesis produces methane, which can be oxidised by oxygen or sulphate. The kinetic rate expressions of all re-oxidation processes are described by standard second-order rate laws (Table S2).

S1.1.3 Isotopic fractionation

To be able to track the isotope compositions of individual Fe compounds, the model contains an extra state variable for each of the Fe compounds. This extra state variable

represents the ^{56}Fe pool of the bulk Fe compounds (e.g., $[^{56}FeS_2]$ is the ^{56}Fe pool of $[FeS_2]$). From the concentration of the ^{56}Fe specific state variables and the bulk state variables, one can then calculate the isotope ratio $^{56}r_{C_i}$ (note that we do not use the capital R notation to avoid confusion with the reaction symbol in Eq. [1]),

$$^{56}r_{C_i} = \frac{^{56}C_i}{C_i - {}^{56}C_i} \quad [10]$$

where $^{56}C_i$ is the concentration of the ^{56}Fe pool of species C_i. Note that we here assume that the Fe isotope pool only consists of ^{56}Fe and ^{54}Fe (the two most abundant iron isotopes). From the isotope ratio, one can calculate the δ^{56}Fe signature,

$$\delta^{56}Fe_{C_i} = \left(\frac{^{56}r_{C_i}}{\left(^{56}Fe / {}^{54}Fe\right)_{ref}} - 1.0 \right) x1000 \quad [11]$$

where $\left(^{56}Fe / {}^{54}Fe\right)_{ref}$ is the isotope ratio of a standard sample (which is defined in the main text). Each individual reaction can be assigned a fractionation factor $^{56}\varepsilon_{R_k}$ (expressed in ‰), which is converted to $^{56}\alpha_{R_k}$,

$$^{56}\alpha_{R_k} = 1 + \frac{^{56}\varepsilon_{R_k}}{1000} \quad [12]$$

Fractionation is then implemented by calculating the reaction for the ^{56}Fe pool from the bulk reaction rate R_k,

$$^{56}R_k = \frac{^{56}\alpha_{R_k}\,{}^{56}r_{C_i}}{1 + {}^{56}\alpha_{R_k}\,{}^{56}r_{C_i}} R_k \quad [13]$$

To avoid extreme fractionations at low bulk concentrations, a fractionation limit is set at 10^{-9} µmol cm^{-3}. Reactions that proceed below this bulk concentration induce no fractionation,

$$^{56}R_k[C_i < 10^{-9}] = \frac{^{56}C_i}{C_i} R_k \quad [15]$$

To account for isotope fractionation during adsorption, the pool of adsorbed ^{56}Fe is calculated as,

$$\left[X \equiv {}^{56}Fe^{2+} \right] = K_{ads}^{Fe^{2+}} \frac{^{56}\alpha_{FIS} + {}^{56}\alpha_{FIS}\,{}^{56}r_{Fe^{2+}}}{1 + {}^{56}\alpha_{FIS}\,{}^{56}r_{Fe^{2+}}} \left[{}^{56}Fe^{2+} \right] \quad [16]$$

where $^{56}\alpha_{FIS}$ is the fractionation factor associated with ferrous iron sorption, and all other parameters have been introduced before.

S1.1.4 Numerical model solution

The numerical solution procedure has been described in detail previously (van de Velde and Meysman, 2016). In brief, the open-source programming language R (R Core Team, 2017) was used to implement a numerical solution procedure for the partial differential

equations by applying the method-of-lines (Boudreau, 1996a) using the R packages CRAN:ReacTran (Soetaert and Meysman, 2012) and CRAN:deSolve (Soetaert et al., 2010b). The sediment grid was generated by dividing the sediment domain (150 cm thickness) into an uneven grid of 200 layers with the thickness of the first layer being 0.015 cm and the thickness of the other layers increasing with a factor 1.018. The resulting set of ordinary differential equations was integrated using the stiff equation solver routine 'vode' (Brown et al., 1989) within the package CRAN:deSolve (Soetaert et al., 2010b). All model simulations were run for a sufficiently long time period (>10,000 year) to allow them to reach a steady state.

Text S2. Early diagenetic model for sensitivity simulation ('generic model')

The second goal of our study was to extend the relation between bottom water oxygen, organic matter oxidation and benthic Fe fluxes proposed by Dale et al. (2015) to include the isotope values of the released Fe. To this end, we constructed a more complex diagenetic model to make sure our results are broadly comparable with the diagenetic model study published previously by Dale et al. (2015). The early diagenetic model used for the sensitivity simulation has the same structure as described above (Eq. [1], Suppl. Text 1.1.1), but with a sediment thickness of 30 cm. The model solving procedure is also identical as described before (Suppl. Text 1.1.4).

S2.1 Diagenetic model formulation

S2.1.1 Model parameterisation: Biogeochemical reaction set

The reaction set (n=37) was reproduced from the diagenetic model of Dale et al. (2015). To account for iron isotope fractionations, an additional set of 15 reactions was included. The biogeochemical reaction set has been described in detail before (Dale et al., 2015). Briefly, organic matter mineralisation was modelled following the classical 'multi-G' (Arndt et al., 2013) approach. The reactive continuum model (Boudreau and Ruddick, 1991) was approximated by 14 different organic matter fractions, each with a different reactivity constant (Dale et al., 2015). Each of these fractions can be degraded by seven different mineralisation pathways; aerobic respiration (AR), denitrification to nitrite (DN_1), denitrification to N_2 (DN_2), manganese reduction (MR), dissimilatory iron reduction (DIR), sulphate reduction (SR) and methanogenesis (MG) (Reactions 1-7; Table S4, note that the same reactions are valid for each of the organic matter fractions). The classical redox sequence (Froelich et al., 1979) is implemented via conventional limitation-inhibition formulations (Table S5; Soetaert et al., 1996).

The nitrogen cycle included in the model is based on previous work by Bohlen et al. (2011). Denitrification proceeds in two separate steps; first nitrate is reduced to nitrite, and subsequently nitrite can be reduced to nitrogen-gas. Aside from denitrification, reduced nitrogen can be produced in the form of ammonium via organic matter mineralisation or via dissimilatory nitrate reduction to ammonium (coupled to sulphide oxidation). Reduced nitrogen in the form of nitrite can be produced via reduction of nitrate coupled to oxidation of iron, or via aerobic oxidation of ammonium. Oxidised nitrogen in the form of nitrate can be produced via aerobic oxidation of nitrite. Furthermore, nitrite and ammonium can combine to form nitrogen-gas via anaerobic ammonium oxidation, and ammonium can adsorb on solid phase particles (Mackin and Aller, 1984).

Manganese oxides are modelled as two separate fractions; highly reactive manganese oxides and moderately reactive manganese oxides (Berg et al., 2003; Dale et al., 2015). Only the highly reactive manganese oxide fraction can be reduced by organic matter mineralisation. Both fractions are reduced by oxidation of ferrous iron and reduced sulphide. Highly reactive manganese oxide is regenerated by oxidation of reduced

manganese by oxygen. Over time, highly reactive manganese oxide ages into moderately reactive manganese oxide (Table S4).

Iron oxides are modelled as four separate fractions; highly reactive iron oxides, moderately reactive iron oxides, poorly reactive iron oxides and unreactive iron oxides, where only the highly reactive iron oxide fraction can reduce organic matter and oxidise sulphide, the other iron oxide fractions only react with sulphide, and the unreactive fraction does not react on diagenetic timescales (Berg et al., 2003; Dale et al., 2015). The classification and reactivity of these iron oxide fractions broadly compare to the classes of reactivities determined in previous laboratory experiments (Canfield et al., 1992; Poulton et al., 2004). Organic matter mineralisation coupled to iron oxide reduction releases ferrous iron (Fe^{2+}) in the pore water, which can (i) adsorb on solid-phase particles, which is implemented as a thermodynamic equilibrium (Eq. 9), (ii) become re-oxidised by oxygen, manganese oxide or nitrate or (iii) precipitate as iron sulphide (Table S4). Over time, highly reactive iron oxide ages into moderately reactive iron oxide.

Sulphate reduction produces free sulphide, which can be (i) re-oxidised by oxygen, (ii) re-oxidised by nitrate, manganese oxide or iron oxide, (iii) precipitated as FeS, (iv) precipitate with FeS to form FeS_2 and hydrogen-gas (Table S4). The oxidation of sulphide by manganese or iron oxides generates elemental sulphur (Poulton, 2003). Elemental sulphur disproportionates into sulphate and sulphide, or reacts with FeS to form FeS_2.

When all electron acceptors are depleted, methanogenesis produces methane, which can be (i) oxidised by oxygen, or (ii) oxidised by sulphate. The kinetic rate expressions of all re-oxidation processes are described by standard second-order rate laws (Table S5).

References for text S1 and S2

Arndt, S., Jørgensen, B. B., LaRowe, D. E., Middelburg, J. J., Pancost, R. D., & Regnier, P. (2013). Quantifying the degradation of organic matter in marine sediments: A review and synthesis. Earth-Science Reviews, 123, 53–86. https://doi.org/10.1016/J.EARSCIREV.2013.02.008

Berg, P., Rysgaard, S., & Thamdrup, B. (2003). Dynamic Modeling of Early Diagenesis and Nutrient Cycling. A Case Study in an Artic Marine Sediment. American Journal of Science, 303(10), 905–955. https://doi.org/10.2475/ajs.303.10.905

Bohlen, L., Dale, A. W., Sommer, S., Mosch, T., Hensen, C., Noffke, A., et al. (2011). Benthic nitrogen cycling traversing the Peruvian oxygen minimum zone. Geochimica et Cosmochimica Acta, 75(20), 6094–6111. https://doi.org/10.1016/j.gca.2011.08.010

Boudreau, B. P. (1984). On the equivalence of nonlocal and radial-diffusion models for porewater irrigation. Journal of Marine Research, 42(3), 731–735. https://doi.org/10.1357/002224084788505924

Boudreau, B. P. (1996a). A method-of-lines code for carbon and nutrient diagenesis in aquatic sediments. Computers & Geosciences, 22(5), 479–496. https://doi.org/10.1016/0098-3004(95)00115-8

Boudreau, B. P. (1996b). The diffusive tortuosity of fine-grained unlithified sediments. Geochimica et Cosmochimica Acta, 60(16), 3139–3142. https://doi.org/10.1016/0016-7037(96)00158-5

Boudreau, B. P. (1997). Diagenetic Models and their Implementation. Springer-Verlag Berlin Heidelberg New York.

Boudreau, B. P. (1998). Mean Mixed Depth of Sediments: the Wherefore and the Why. Limnology and Oceanography, 43(3), 524–526.

Boudreau, B. P., & Ruddick, B. R. (1991). On a reactive continuum representation of organic matter diagenesis. American Journal of Science, 291(5), 507–538. https://doi.org/10.2475/ajs.291.5.507

Brown, P., Byrne, G., & Hindmarsh, A. (1989). VODE, a variable-coefficient ODE solver. SIAM J Sci Stat Comput, 10, 1038–1051.

Canfield, D. E., Raiswell, R., & Bottrell, S. H. (1992). The reactivity of sedimentary iron minerals toward sulfide. American Journal of Science, 292, 659–683.

Van Cappellen, P., & Wang, Y. (1995). Metal cycling in surface sediments: Modeling the interplay of transport and reaction. In H. E. Allen (Ed.), Metal Contaminated Aquatic Sediments (pp. 21–64). Ann Arbor Press.

Dale, A. W., Nickelsen, L., Scholz, F., Hensen, C., Oschlies, A., & Wallmann, K. (2015). A revised global estimate of dissolved iron fluxes from marine sediments. Global Biogeochemical Cycles, 29, 1–17. https://doi.org/10.1002/2013GB004679.Received

Dauphas, N., John, S. G., & Rouxel, O. (2017). Iron isotope systematics. Reviews in Mineralogy & Geochemistry, 82, 415–510. https://doi.org/10.2138/rmg.2017.82.11

Fick, A. (1855). Uber Diffusion. Annals of Physics, 94, 59–86.

Froelich, P. N., Klinkhammer, G. P., Bender, M. L., Luedtke, N. A., Heath, G. R., Cullen, D., et al. (1979). Early oxidation of organic matter in pelagic sediments of the eastern

equatorial Atlantic: suboxic diagenesis. Geochimica et Cosmochimica Acta, 43, 1075–1090.
Kristensen, E., Røy, H., Debrabant, K., & Valdemarsen, T. (2018). Carbon oxidation and bioirrigation in sediments along a Skagerrak–Kattegat–Belt Sea depth transect. Marine Ecology Progress Series, 604, 33–50. https://doi.org/10.3354/meps12734
Mackin, J. E., & Aller, R. C. (1984). Ammonium adsorption in marine sediments. Limnology and Oceanography, 29(2), 250–257. https://doi.org/10.4319/lo.1984.29.2.0250
Meile, C., Berg, P., Van Cappellen, P., & Tuncay, K. (2005). Solute-specific pore water irrigation: Implications for chemical cycling in early diagenesis. Journal of Marine Research, 63, 601–621. https://doi.org/10.1357/0022240054307885
Meysman, F. J. R., Middelburg, J. J., Herman, P. M. J., & Heip, C. H. R. (2003). Reactive transport in surface sediments. II. Media: an object-oriented problem-solving environment for early diagenesis. Computers & Geosciences, 29(3), 301–318. https://doi.org/10.1016/S0098-3004(03)00007-4
Meysman, F. J. R., Boudreau, B. P., & Middelburg, J. J. (2005). Modeling reactive transport in sediments subject to bioturbation and compaction. Geochimica et Cosmochimica Acta, 69(14), 3601–3617. https://doi.org/10.1016/j.gca.2005.01.004
Meysman, F. J. R., Boudreau, B. P., & Middelburg, J. J. (2010). When and why does bioturbation lead to diffusive mixing? Journal of Marine Research, 68, 881–920.
Meysman, F. J. R., Risgaard-Petersen, N., Malkin, S. Y., & Nielsen, L. P. (2015). The geochemical fingerprint of microbial long-distance electron transport in the seafloor. Geochimica et Cosmochimica Acta, 152, 122–142. https://doi.org/10.1016/j.gca.2014.12.014
Middelburg, J. J. (2019). Marine Carbon Biogeochemistry. In Marine Carbon Biogeochemistry. A primer for Earth System Scientists. Springer Nature Switzerland AG. https://doi.org/10.1007/978-3-030-10822-9
Poulton, S. W. (2003). Sulfide oxidation and iron dissolution kinetics during the reaction of dissolved sulfide with ferrihydrite. Chemical Geology, 202(1–2), 79–94. https://doi.org/10.1016/S0009-2541(03)00237-7
Poulton, S. W., & Canfield, D. E. (2005). Development of a sequential extraction procedure for iron: Implications for iron partitioning in continentally derived particulates. Chemical Geology, 214, 209–221. https://doi.org/10.1016/j.chemgeo.2004.09.003
Poulton, S. W., Krom, M. D., & Raiswell, R. (2004). A revised scheme for the reactivity of iron (oxyhydr)oxide minerals towards dissolved sulfide. Geochimica et Cosmochimica Acta, 68(18), 3703–3715. https://doi.org/10.1016/j.gca.2004.03.012
R Core Team. (2017). R: A Language and Environment for Statistical Computing.
Reimers, C. E., Ruttenberg, K. C., Canfield, D. E., Christiansen, M. B., & Martin, J. B. (1996). Porewater pH and authigenic phases formed in the uppermost sediments of the Santa Barbara Basin. Geochimica et Cosmochimica Acta, 60(21), 4037–4057. https://doi.org/10.1016/S0016-7037(96)00231-1
Rickard, D. (1975). Kinetics and mechanism of pyrite formation at low temperatures. American Journal of Science, 275, 636–652.

Rickard, D. (1997). Kinetics of pyrite formation by the H2S oxidation of iron (II) monosulfide in aqueous solutions between 25 and 125°C: The rate equation. Geochimica et Cosmochimica Acta, 61(1), 115–134. https://doi.org/10.1016/s0016-7037(96)00321-3

Severmann, S., Johnson, C. M., Beard, B. L., & McManus, J. (2006). The effect of early diagenesis on the Fe isotope compositions of porewaters and authigenic minerals in continental margin sediments. Geochimica et Cosmochimica Acta, 70(8), 2006–2022. https://doi.org/10.1016/j.gca.2006.01.007

Soetaert, K., & Meysman, F. (2012). Reactive transport in aquatic ecosystems: Rapid model prototyping in the open source software R. Environmental Modelling and Software, 32, 49–60. https://doi.org/10.1016/j.envsoft.2011.08.011

Soetaert, K., Herman, P. M. J., & Middelburg, J. J. (1996). A model of early diagenetic processes from the shelf To abyssal depths. Geochimica et Cosmochimica Acta, 60(6), 1019–1040.

Soetaert, K., Petzoldt, T., & Meysman, F. J. R. (2010). marelac: Tools for Aquatic Sciences R package version 2.1.

Soetaert, K., Petzoldt, T., & Setzer, R. W. (2010). Package deSolve: Solving Initial Value Differential Equations in R. Journal Of Statistical Software, 33(9), 1–25. Retrieved from http://www.jstatsoft.org/v33/i09/paper

van de Velde, S. J., & Meysman, F. J. R. (2016). The influence of bioturbation on iron and sulphur cycling in marine sediments: a model analysis. Aquatic Geochemistry, 22(5–6), 469–504. https://doi.org/10.1007/s10498-016-9301-7

van de Velde, S. J., Hidalgo-Martinez, S., Callebaut, I., Antler, G., James, R., Leermakers, M., & Meysman, F. (2020). Burrowing fauna mediate alternative stable states in the redox cycling of salt marsh sediments. Geochimica et Cosmochimica Acta, 276, 31–49. https://doi.org/10.1016/j.gca.2020.02.021

Wang, Y., & Van Cappellen, P. (1996). A multicomponent reactive transport model of early diagenesis: Application to redox cycling in coastal marine sediments. Geochimica et Cosmochimica Acta, 60(16), 2993–3014. https://doi.org/10.1016/0016-7037(96)00140-8

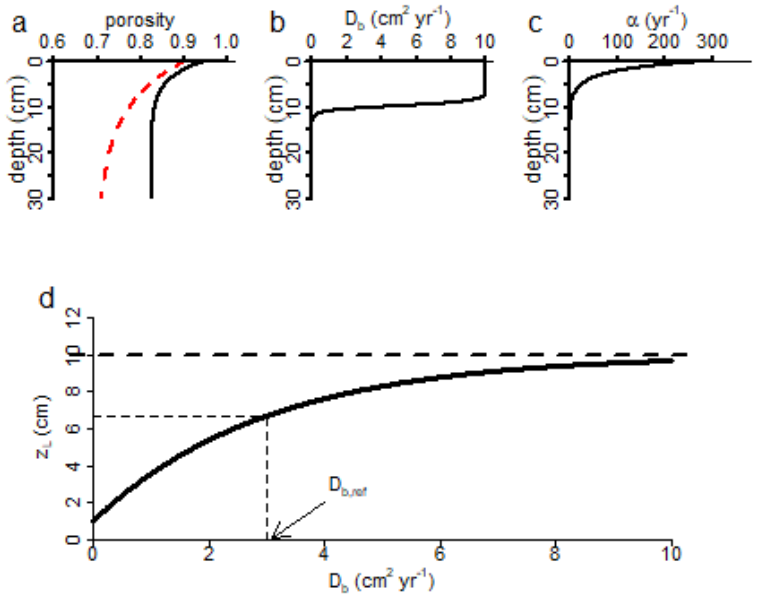

Figure S1: (a) Porosity profile (black line is the applied porosity profile for the model calibration, red dashed line is the generic porosity profile for all other model runs), (b) bio-diffusion profile, (c) bio-irrigation profile for the baseline simulation. (d) Relation between $D_{b,0}$ and z_L, as proposed by van de Velde and Meysman (2016).

	Kinetic reactions	
R1	Aerobic respiration	$CH_2O_i + O_2 \rightarrow HCO_3^- + H^+ \quad (i = 1,...,14)$
R2	Dissimilatory Iron reduction	$CH_2O_i + 4FeOOH_f + 7H^+ \rightarrow HCO_3^- + 4Fe^{2+} + 6H_2O \quad (i = 1,...,14)$
R3	Sulphate reduction	$CH_2O_i + \frac{1}{2}SO_4^{2-} \rightarrow HCO_3^- + \frac{1}{2}HS^- + \frac{1}{2}H^+ \quad (i = 1,...,14)$
R4	Methanogenesis	$CH_2O_i + \frac{1}{2}H_2O \rightarrow \frac{1}{2}HCO_3^- + \frac{1}{2}CH_4 + \frac{1}{2}H^+ \quad (i = 1,...,14)$
R5	Ferrous iron oxidation	$Fe^{2+} + \frac{1}{4}O_2 + \frac{3}{2}H_2O \rightarrow FeOOH_f + 2H^+$
R5b	Adsorbed iron oxidation	$X \equiv Fe^{2+} + \frac{1}{4}O_2 + \frac{3}{2}H_2O \rightarrow FeOOH_f + 2H^+$
R6	Canonical sulphur oxidation	$HS^- + 2O_2 \rightarrow SO_4^{2-} + H^+$
R7	Aerobic methane oxidation	$CH_4 + 2O_2 \rightarrow CO_2 + 2H_2O$
R8	Iron sulphide oxidation	$FeS + \frac{9}{4}O_2 + \frac{3}{2}H_2O \rightarrow FeOOH_f + SO_4^{2-} + 2H^+$
R9	Pyrite oxidation	$FeS_2 + \frac{15}{4}O_2 + \frac{5}{2}H_2O \rightarrow 2SO_4^{2-} + FeOOH_f + 4H^+$
R10	Sulphide-mediated iron reduction	$HS^- + 8FeOOH_{f,a} + 7H^+ \rightarrow SO_4^{2-} + 8Fe^{2+} + 12H_2O$
R11	Anaerobic methane oxidation	$CH_4 + SO_4^{2-} \rightarrow HCO_3^- + HS^- + H_2O$
R12	Ferrous iron sorption	$Fe^{2+} \leftrightarrow X \equiv Fe^{2+}$
R13	Iron sulphide precipitation	$Fe^{2+} + HS^- \rightarrow FeS + H^+$
R14	Iron sulphide dissolution	$FeS + H^+ \rightarrow Fe^{2+} + HS^-$
R15	Pyrite precipitation	$FeS + \frac{3}{4}HS^- + \frac{1}{4}SO_4^{2-} + \frac{7}{4}H^+ \rightarrow FeS_2 + H_2O$
R16	Iron oxide ageing	$FeOOH_f \rightarrow FeOOH_a$

Table S1. List of biogeochemical reactions included in the reaction-transport model used for calibration of the isotope fractionation factors.

	Kinetic rate expression
	$R_{\min} = \varphi_S \sum_{i=1}^{14} k_{\min,i} \left[CH_2O_i\right]$
R1	$R = R_{\min} \frac{\left[O_2\right]}{\left[O_2\right] + K_{O_2}}$
R2	$R = R_{\min} \frac{K_{O_2}}{\left[O_2\right] + K_{O_2}} \frac{\left[FeOOH_f\right]}{\left[FeOOH_f\right] + K_{FeOOH}}$
R3	$R = R_{\min} \frac{K_{O_2}}{\left[O_2\right] + K_{O_2}} \frac{K_{FeOOH}}{\left[FeOOH_f\right] + K_{FeOOH}} \frac{\left[SO_4^{2-}\right]}{\left[SO_4^{2-}\right] + K_{SO_4^{2-}}}$
R4	$R = R_{\min} \frac{K_{O_2}}{\left[O_2\right] + K_{O_2}} \frac{K_{FeOOH}}{\left[FeOOH_f\right] + K_{FeOOH}} \frac{K_{SO_4^{2-}}}{\left[SO_4^{2-}\right] + K_{SO_4^{2-}}}$
R5a	$R = \varphi_F k_{FIO} \left[Fe^{2+}\right]\left[O_2\right]$
R5b	$R = \varphi_S k_{FIO} \left[X \equiv Fe^{2+}\right]\left[O_2\right]$
R6	$R = \varphi_F k_{CSO} \left[HS^-\right]\left[O_2\right]$
R7	$R = \varphi_F k_{AMO} \left[CH_4\right]\left[O_2\right]$
R8	$R = \varphi_S k_{ISO} \left[FeS\right]\left[O_2\right]$
R9	$R = \varphi_S k_{PyO} \left[FeS_2\right]\left[O_2\right]$
R10	$R = \varphi_S k_{SMI} \left[HS^-\right]\left[FeOOH_{f,a}\right]$
R11	$R = \varphi_F k_{AnMO} \left[CH_4\right]\left[SO_4^{2-}\right]$
R12	$R = \varphi_F k_{ISP} \left(\frac{[Fe^{2+}][HS^-]}{[H^+]K_{FeS}^{SP}} - 1 \right)$
R13	$R = \varphi_s k_{ISD} [FeS] \left(1 - \frac{[Fe^{2+}][HS^-]}{[H^+]K_{FeS}^{SP}} \right)$
R14	$R = \varphi_S k_{PyP} \left[FeS\right]\left[HS^-\right]$
R15	$R = \varphi_S k_{IOA} \left[FeOOH_f\right]$

Table S2. List of kinetic expressions included in the reaction-transport model used for calibration of the isotope fractionation factors.

ENVIRONMENTAL PARAMETERS	**Symbol**	**Value**		**Units**	**Method**	**References**
		SBB	**MC**			
Temperature	T	10	10	ºC	A	[1],[2]
Salinity	S	34.2	34.2	-	A	[1],[2]
Porosity (surface value)	ϕ_F^0	0.948	0.948	-	A	[1],[2]
Porosity (asymptotic at depth)	ϕ_F^∞	0.824	0.824	-	A	[1],[2]
Porosity attenuation coefficient	x_ϕ	3.6	3.6	cm	A	[1],[2]
Solid-phase density	ρ_S	2.6	2.6	g cm^{-3}	A	[1],[2]
Sediment accumulation rate at infinite depth	v_S, v_F	250	250	cm kyr^{-1}	A	[3]
Depth of sediment domain	L	150	150	cm	-	
$^{56}Fe/^{54}Fe$ isotope ratio of IRMM014	-	15.697861		-	A	[4]
BOUNDARY CONDITIONS	**Symbol**	**Value**		**Units**	**Method**	**References**
Oxygen bottom water	$[O_2]$	0.01	0.28	mol m^{-3}	A	[1]-[3]
Sulphate bottom water	$[SO_4^{2-}]$	28.0	28.0	mol m^{-3}	A	[1]-[3]
DIC bottom water	$\sum CO_2$	2.45	2.45	mol m^{-3}	A	[1],[2]
Ferrous iron bottom water	$[Fe^{2+}]$	0	0	mol m^{-3}	A	[1],[2]
Free sulphide bottom water	$[HS^-]$	0	0	mol m^{-3}	A	[1],[2]
Methane bottom water	$[CH_4]$	0	0	mol m^{-3}	A	[1],[2]
Flux POC	J_{POC}	4.6	8.0	mmol m^{-2} d^{-1}	B	
Flux $FeOOH_T$	$J_{FeOOH,T}$	560	320	µmol m^{-2} d^{-1}	B	
Isotopic signature	$\delta^{56}Fe_{FeOOH}$	-1.5	-0.5	‰	B	
Flux FeS	J_{FeS}	0	0	mmol m^{-2} d^{-1}	B	
Isotopic signature	$\delta^{56}Fe_{FeS}$	-	-	‰	B	
Flux FeS_2	J_{FeS2}	0.03	0.03	mmol m^{-2} d^{-1}	B	
Isotopic signature	$\delta^{56}Fe_{FeS2}$	-0.4	0.0	‰	B	

[1]This value is only for the 'fresh' fraction, the flux of the 'aged' fraction was set to 0.

Table S3: List of boundary conditions and parameters used in the reaction-transport model used for calibration of the isotope fractionation factors. Solid-phase concentrations are expressed per unit volume of solid phase. "Method" refers to the procedure by which parameter values are constrained: A = Literature values, B = model calibration. Note that all isotope values are given relative to the IRMM-14 standard.
References: [1] Reimers et al. (1996), [2] Meysman et al. (2005), [3] Severmann et al. (2006), [4] Dauphas et al., (2017), [5] Dale et al. (2015), [6] van de Velde and Meysman (2016), [7] Poulton and Canfield, (2005) [8] Meysman et al. (2015), [9] Rickard (1975), [10] van de Velde et al. (2020), [11] Berg et al. (2003).

BIOGEOCHEMICAL PARAMETERS	Symbol	Value		Units	Method	References
		SBB	MC			
Mixing depth	z_L	0	10	cm	B	
Biodiffusion coefficient	$D_{b,0}$	0	20	$cm^2\ yr^{-1}$	B	
Bio-irrigation coefficient	α_0	0	183	yr^{-1}	B	
Bio-irrigation attenuation coefficient	x_{irr}	0	3	cm	B	
Mineralisation constants	$k_{\min,1}$	10^{-10}	2.0	yr^{-1}	A	[2],[5]
	$k_{\min,2}$	$3.16\ 10^{-10}$	0.056	yr^{-1}	A	[2],[5]
	$k_{\min,3}$	$3.16\ 10^{-9}$	$1.1\ 10^{-4}$	yr^{-1}	A	[2],[5]
	$k_{\min,4}$	$3.16\ 10^{-8}$	0	yr^{-1}	A	[5]
	$k_{\min,5}$	$3.16\ 10^{-7}$	0	yr^{-1}	A	[5]
	$k_{\min,6}$	$3.16\ 10^{-6}$	0	yr^{-1}	A	[5]
	$k_{\min,7}$	$3.16\ 10^{-5}$	0	yr^{-1}	A	[5]
	$k_{\min,8}$	$3.16\ 10^{-4}$	0	yr^{-1}	A	[5]
	$k_{\min,9}$	$3.16\ 10^{-3}$	0	yr^{-1}	A	[5]
	$k_{\min,10}$	$3.16\ 10^{-2}$	0	yr^{-1}	A	[5]
	$k_{\min,11}$	$3.16\ 10^{-1}$	0	yr^{-1}	A	[5]
	$k_{\min,12}$	3.16	0	yr^{-1}	A	[5]
	$k_{\min,13}$	31.6	0	yr^{-1}	A	[5]
	$k_{\min,14}$	100	0	yr^{-1}	A	[5]
Oxygen saturation constant	K_{O_2}	0.001		$mol\ m^{-3}$	A	[2]
FeOOH saturation constant	K_{FeOOH}	31.2	1.04	$mol\ m^{-3}$	B	
Sulphate saturation constant	$K_{SO_4^{2-}}$	0.9		$mol\ m^{-3}$	A	[2]
Ferrous iron oxidation	k_{FIO}	10^{+7}		$\mu mol^{-1}\ cm^3\ yr^{-1}$	A	[2]
Canonical sulphur oxidation	k_{CSO}	10^{+7}		$\mu mol^{-1}\ cm^3\ yr^{-1}$	A	[2]
Aerobic methane oxidation	k_{AMO}	10^{+4}		$\mu mol^{-1}\ cm^3\ yr^{-1}$	A	[2]
Iron sulphide oxidation	k_{ISO}	10^{+7}		$\mu mol^{-1}\ cm^3\ yr^{-1}$	A	[2]
Pyrite oxidation	k_{PyO}	9.47		$\mu mol^{-1}\ cm^3\ yr^{-1}$	A	[5]
Sulphide-mediated iron reduction	$k_{SMI,f}$	494		$\mu mol^{-1}\ cm^3\ yr^{-1}$	A	[6],[7]
Sulphide-mediated iron reduction	$k_{SMI,a}$	3		$\mu mol^{-1}\ cm^3\ yr^{-1}$	A	[6],[7]
Anaerobic methane oxidation	k_{AnMO}	10^{+2}		$\mu mol^{-1}\ cm^3\ yr^{-1}$	A	[2]
Equilibrium constant ferrous iron sorption	$K_{ads}^{Fe^{2+}}$	69.68		-	B	-
Iron sulphide precipitation	k_{ISP}	10^{+4}		$\mu mol\ cm^3\ yr^{-1}$	A	[8]
Iron sulphide dissolution	k_{ISD}	3		yr^{-1}	A	[8]
Pyrite precipitation	k_{PyP}	3.25		$\mu mol^{-1}\ cm^3\ yr^{-1}$	A	[9],[10]
Iron oxide ageing	k_{IOA}	0.6		yr^{-1}	A	[11]

Table S3 continued

	Kinetic reactions	
R1	Aerobic respiration	$CH_2O_i.\{NH_4^+\}_{r_{NC}} + O_2 \rightarrow HCO_3^- + r_{NC}NH_4^+ + H^+ \quad (i = 1,...,14)$
R2	Denitrification	$CH_2O_i.\{NH_4^+\}_{r_{NC}} + 2NO_3^- \rightarrow HCO_3^- + 2NO_2^- + r_{NC}NH_4^+ + H^+ (i = 1,...,14)$
R3	Denitrification	$CH_2O_i.\{NH_4^+\}_{r_{NC}} + \frac{4}{3}NO_2^- + \frac{1}{3}H^+ \rightarrow HCO_3^- + \frac{2}{3}N_2 + r_{NC}NH_4^+ + \frac{2}{3}H_2O (i = 1,...,14)$
R4	Manganese reduction	$CH_2O_i.\{NH_4^+\}_{r_{NC}} + 2MnO_{2HR} + 3H^+ \rightarrow HCO_3^- + 2Mn^{2+} + r_{CN}NH_4^+ + 2H_2O \quad (i = 1,...,14)$
R5	Dissimilatory Iron reduction	$CH_2O_i.\{NH_4^+\}_{r_{NC}} + 4FeOOH_{HR} + 7H^+ \rightarrow HCO_3^- + 4Fe^{2+} + r_{CN}NH_4^+ + 6H_2O \quad (i = 1,...,14)$
R6	Sulphate reduction	$CH_2O_i.\{NH_4^+\}_{r_{NC}} + \frac{1}{2}SO_4^{2-} \rightarrow HCO_3^- + \frac{1}{2}HS^- + r_{CN}NH_4^+ + \frac{1}{2}H^+ \quad (i = 1,...,14)$
R7	Methanogenesis	$CH_2O_i.\{NH_4^+\}_{r_{NC}} + \frac{1}{2}H_2O \rightarrow \frac{1}{2}HCO_3^- + \frac{1}{2}CH_4 + r_{CN}NH_4^+ + \frac{1}{2}H^+ \quad (i = 1,...,14)$
R8	H_2 oxidation with O_2	$H_2 + \frac{1}{2}O_2 \rightarrow H_2O$
R9	H_2 oxidation with NO_3^-	$H_2 + NO_3^- \rightarrow H_2O + NO_2^-$
R10	H_2 oxidation with NO_2^-	$H_2 + \frac{2}{3}NO_2^- + \frac{2}{3}H^+ \rightarrow \frac{4}{3}H_2O + \frac{1}{3}N_2$
R11	H_2 oxidation with MnO_2	$H_2 + MnO_{2HR} + 2H^+ \rightarrow 2H_2O + Mn^{2+}$
R12	H_2 oxidation with FeOOH	$H_2 + 2FeOOH_{HR} + 4H^+ \rightarrow 4H_2O + 2Fe^{2+}$
R13	H_2 oxidation with SO_4^{2-}	$H_2 + \frac{1}{4}SO_4^{2-} + \frac{1}{4}H^+ \rightarrow H_2O + \frac{1}{4}HS^-$
R14	Nitrification	$NH_4^+ + \frac{3}{2}O_2 \rightarrow NO_2^- + H_2O + 2H^+$
R15	Nitrification	$NO_2^- + \frac{1}{2}O_2 \rightarrow NO_3^-$
R16	Manganese oxidation	$Mn^{2+} + \frac{1}{2}O_2 + H_2O \rightarrow MnO_{2HR} + 2H^+$
R17	Ferrous iron oxidation	$Fe^{2+} + \frac{1}{4}O_2 + \frac{3}{2}H_2O \rightarrow FeOOH_{HR} + 2H^+$
R17b	Adsorbed iron oxidation	$X \equiv Fe^{2+} + \frac{1}{4}O_2 + \frac{3}{2}H_2O \rightarrow FeOOH_{HR} + 2H^+$
R18	Canonical sulphur oxidation	$HS^- + 2O_2 \rightarrow SO_4^{2-} + H^+$
R19	Aerobic methane oxidation	$CH_4 + 2O_2 \rightarrow CO_2 + 2H_2O$
R20	Iron sulphide oxidation	$FeS + \frac{9}{4}O_2 + \frac{3}{2}H_2O \rightarrow FeOOH_{HR} + SO_4^{2-} + 2H^+$
R21	Pyrite oxidation	$FeS_2 + \frac{15}{4}O_2 + \frac{5}{2}H_2O \rightarrow 2SO_4^{2-} + FeOOH_{HR} + 4H^+$
R22	Anaerobic ammonium oxidation	$NH_4^+ + NO_2^- \rightarrow N_2 + 2H_2O$
R23	Iron-mediated nitrate reduction	$Fe^{2+} + \frac{1}{5}NO_3^- + \frac{7}{5}H_2O \rightarrow FeOOH_{HR} + \frac{1}{10}N_2 + \frac{9}{5}H^+$

R24	Sulphide-mediated nitrate reduction	$HS^- + NO_3^- + H_2O + H^+ \rightarrow SO_4^{2-} + NH_4^+$
R25	Iron-mediated manganese reduction	$Fe^{2+} + \frac{1}{2} MnO_{2HR,MR} + H_2O \rightarrow FeOOH_{HR} + \frac{1}{2} Mn^{2+} + H^+$
R26	Sulphide-mediated manganese reduction	$HS^- + MnO_{2HR,MR} + 3H^+ \rightarrow S^0 + Mn^{2+} + 2H_2O$
R27	Sulphide-mediated iron reduction	$HS^- + 2FeOOH_{HR,MR,PR} + 5H^+ \rightarrow S^0 + 2Fe^{2+} + 4H_2O$
R28	Anaerobic methane oxidation	$CH_4 + SO_4^{2-} \rightarrow HCO_3^- + HS^- + H_2O$
R29	Ammonium sorption	$NH_4^+ \leftrightarrow X \equiv NH_4^+$
R30	Ferrous iron sorption	$Fe^{2+} \leftrightarrow X \equiv Fe^{2+}$
R31	Elemental sulphur disproportionation	$S^0 + H_2O \rightarrow \frac{1}{4} SO_4^{2-} + \frac{3}{4} HS^- + \frac{5}{4} H^+$
R32	Iron sulphide precipitation	$Fe^{2+} + HS^- \rightarrow FeS + H^+$
R33	Iron sulphide dissolution	$FeS + H^+ \rightarrow Fe^{2+} + HS^-$
R34	Pyrite precipitation	$FeS + HS^- + H^+ \rightarrow FeS_2 + H_2$
R35	Pyrite precipitation	$FeS + S^0 \rightarrow FeS_2$
R36	Manganese oxide ageing	$MnO_{2HR} \rightarrow MnO_{2MR}$
R37	Iron oxide ageing	$FeOOH_{HR} \rightarrow FeOOH_{MR}$

Table S4 List of biogeochemical reactions included in the reaction-transport model used for the sensitivity simulation.

	Kinetic rate expression
	$R_{\min} = \varphi_S \sum_{i=1}^{14} k_{\min,i} \left[CH_2O_i\right] / R_{H_2} = \varphi_F k_{H_2} \left[H_2\right]$
R1	$R = R_{\min} \frac{\left[O_2\right]}{\left[O_2\right] + K_{O_2}}$
R2	$R = R_{\min} \frac{K_{O_2}}{\left[O_2\right] + K_{O_2}} \frac{\left[NO_3^-\right]}{\left[NO_3^-\right] + K_{NO_3^-}}$
R3	$R = R_{\min} \frac{K_{O_2}}{\left[O_2\right] + K_{O_2}} \frac{K_{NO_3^-}}{\left[NO_3^-\right] + K_{NO_3^-}} \frac{\left[NO_2^-\right]}{\left[NO_2^-\right] + K_{NO_2^-}}$
R4	$R = R_{\min} \frac{K_{O_2}}{\left[O_2\right] + K_{O_2}} \frac{K_{NO_3^-}}{\left[NO_3^-\right] + K_{NO_3^-}} \frac{K_{NO_2^-}}{\left[NO_2^-\right] + K_{NO_2^-}} \frac{\left[MnO_{2HR}\right]}{\left[MnO_{2HR}\right] + K_{MnO_2}}$
R5	$R = R_{\min} \frac{K_{O_2}}{\left[O_2\right] + K_{O_2}} \frac{K_{NO_3^-}}{\left[NO_3^-\right] + K_{NO_3^-}} \frac{K_{NO_2^-}}{\left[NO_2^-\right] + K_{NO_2^-}} \frac{K_{MnO_2}}{\left[MnO_{2HR}\right] + K_{MnO_2}} \frac{\left[FeOOH_{HR}\right]}{\left[FeOOH_{HR}\right] + K_{FeOOH}}$
R6	$R = R_{\min} \frac{K_{O_2}}{\left[O_2\right] + K_{O_2}} \frac{K_{NO_3^-}}{\left[NO_3^-\right] + K_{NO_3^-}} \frac{K_{NO_2^-}}{\left[NO_2^-\right] + K_{NO_2^-}} \frac{K_{MnO_2}}{\left[MnO_{2HR}\right] + K_{MnO_2}} \frac{K_{FeOOH}}{\left[FeOOH_{HR}\right] + K_{FeOOH}} \frac{\left[SO_4^{2-}\right]}{\left[SO_4^{2-}\right] + K_{SO_4^{2-}}}$
R7	$R = R_{\min} \frac{K_{O_2}}{\left[O_2\right] + K_{O_2}} \frac{K_{NO_3^-}}{\left[NO_3^-\right] + K_{NO_3^-}} \frac{K_{NO_2^-}}{\left[NO_2^-\right] + K_{NO_2^-}} \frac{K_{MnO_2}}{\left[MnO_{2HR}\right] + K_{MnO_2}} \frac{K_{FeOOH}}{\left[FeOOH_{HR}\right] + K_{FeOOH}} \frac{K_{SO_4^{2-}}}{\left[SO_4^{2-}\right] + K_{SO_4^{2-}}}$
R8	$R = R_{H_2} \frac{\left[O_2\right]}{\left[O_2\right] + K_{O_2}}$
R9	$R = R_{H_2} \frac{K_{O_2}}{\left[O_2\right] + K_{O_2}} \frac{\left[NO_3^-\right]}{\left[NO_3^-\right] + K_{NO_3^-}}$
R10	$R = R_{H_2} \frac{K_{O_2}}{\left[O_2\right] + K_{O_2}} \frac{K_{NO_3^-}}{\left[NO_3^-\right] + K_{NO_3^-}} \frac{\left[NO_2^-\right]}{\left[NO_2^-\right] + K_{NO_2^-}}$
R11	$R = R_{H_2} \frac{K_{O_2}}{\left[O_2\right] + K_{O_2}} \frac{K_{NO_3^-}}{\left[NO_3^-\right] + K_{NO_3^-}} \frac{K_{NO_2^-}}{\left[NO_2^-\right] + K_{NO_2^-}} \frac{\left[MnO_{2HR}\right]}{\left[MnO_{2HR}\right] + K_{MnO_2}}$
R12	$R = R_{H_2} \frac{K_{O_2}}{\left[O_2\right] + K_{O_2}} \frac{K_{NO_3^-}}{\left[NO_3^-\right] + K_{NO_3^-}} \frac{K_{NO_2^-}}{\left[NO_2^-\right] + K_{NO_2^-}} \frac{K_{MnO_2}}{\left[MnO_{2HR}\right] + K_{MnO_2}} \frac{\left[FeOOH_{HR}\right]}{\left[FeOOH_{HR}\right] + K_{FeOOH}}$
R13	$R = R_{H_2} \frac{K_{O_2}}{\left[O_2\right] + K_{O_2}} \frac{K_{NO_3^-}}{\left[NO_3^-\right] + K_{NO_3^-}} \frac{K_{NO_2^-}}{\left[NO_2^-\right] + K_{NO_2^-}} \frac{K_{MnO_2}}{\left[MnO_{2HR}\right] + K_{MnO_2}} \frac{K_{FeOOH}}{\left[FeOOH_{HR}\right] + K_{FeOOH}} \frac{\left[SO_4^{2-}\right]}{\left[SO_4^{2-}\right] + K_{SO_4^{2-}}}$
R14	$R = \varphi_F k_{NIT.1} \left[NH_4^+\right] \left[O_2\right]$
R15	$R = \varphi_F k_{NIT.2} \left[NO_2^-\right] \left[O_2\right]$
R16	$R = \varphi_F k_{MnO} \left[Mn^{2+}\right] \left[O_2\right]$
R17a	$R = \varphi_F k_{FIO} \left[Fe^{2+}\right] \left[O_2\right]$
R17b	$R = \varphi_S k_{FIO} \left[X \equiv Fe^{2+}\right] \left[O_2\right]$
R18	$R = \varphi_F k_{CSO} \left[HS^-\right] \left[O_2\right]$
R19	$R = \varphi_F k_{AMO} \left[CH_4\right] \left[O_2\right]$

R20 $R = \varphi_S k_{ISO} [FeS][O_2]$

R21 $R = \varphi_S k_{PyO} [FeS_2][O_2]$

R22 $R = \varphi_F k_{ANA} \left[NH_4^+ \right] \left[NO_2^- \right]$

R23 $R = \varphi_F k_{NFO} \left[Fe^{2+} \right] \left[NO_3^- \right]$

R24 $R = \varphi_F k_{NSO} \left[HS^- \right] \left[NO_3^- \right]$

R25 $R = \varphi_S k_{MFO} \left[Fe^{2+} \right] \left[MnO_{2HR,MR} \right]$

R26 $R = \varphi_S k_{MsO} \left[HS^- \right] \left[MnO_{2HR,MR} \right]$

R27 $R = \varphi_S k_{SMI} \left[HS^- \right]^{1/2} \left[FeOOH_{HR,MR,PR} \right]$

R28 $R = \varphi_F k_{AnMO} \left[CH_4 \right] \left[SO_4^{2-} \right]$

R29 $R = \varphi_F k_{AmS} \left(1 - \frac{\left[X \equiv NH_4^+ \right]}{K_{ads}^{NH_4^+} \left[NH_4^+ \right]} \right)$

R31 $R = \varphi_F k_{SDP} \left[S^0 \right]$

R32 $R = \varphi_S k_{ISP} [Fe^{2+}][HS^-]$

R33 $R = \varphi_s k_{ISD} [FeS] \left(1 - \frac{[Fe^{2+}][HS^-]}{[H^+] K_{FeS}^{SP}} \right)^{n_{ISD}}$

R34 $R = \varphi_S k_{PyP.1} \left[FeS \right] \left[HS^- \right]$

R35 $R = \varphi_S k_{PyP.2} \left[FeS \right] \left[S^0 \right]$

R36 $R = \varphi_S k_{MOA} \left[MnO_{2HR} \right]$

R37 $R = \varphi_S k_{IOA} \left[FeOOH_{HR} \right]$

Table S5 List of kinetic expressions included in the reaction-transport model used for the sensitivity simulation.

ENVIRONMENTAL PARAMETERS	**Symbol**	**Value**	**Units**	**Method**	**References**
Temperature	T	10	ºC	A	[1]
Salinity	S	34.2	-	A	[1]
Porosity (surface value)	ϕ_F^0	0.9	-	A	[1]
Porosity (asymptotic at depth)	ϕ_F^∞	0.7	-	A	[1]
Porosity attenuation coefficient	x_ϕ	10.0	cm	A	[1]
Solid-phase density	ρ_S	2.6	g cm^{-3}	A	[1]
Sediment accumulation rate at infinite depth	v_S, v_F	60	cm kyr^{-1}	A	[1]
Depth of sediment domain	L	30	cm	A	[1]
$^{56}Fe/^{54}Fe$ isotope ratio of IRMM014	-	15.697861	-	A	[2]
BOUNDARY CONDITIONS	**Symbol**	**Value**	**Units**	**Method**	**References**
Oxygen bottom water	$[O_2]$	variable	mol m^{-3}	-	
Nitrate bottom water	$[NO_3^-]$	0.035	mol m^{-3}	A	[1]
Sulphate bottom water	$[SO_4^{2-}]$	28.0	mol m^{-3}	-	-
DIC bottom water	$\sum CO_2$	2.2	mol m^{-3}	-	-
Ammonium bottom water	$[NH_4^+]$	0.001	mol m^{-3}	A	[1]
Manganese bottom water	$[Mn^{2+}]$	0	mol m^{-3}	A	[1]
Ferrous iron bottom water	$[Fe^{2+}]$	0	mol m^{-3}	A	[1]
Free sulphide bottom water	$[HS^-]$	0	mol m^{-3}	A	[1]
Methane bottom water	$[CH_4]$	0	mol m^{-3}	A	[1]
Flux POC	J_{POC}	variable	mmol m^{-2} d^{-1}	-	
Flux MnO_2 [1]	F_{MnO2}	108	µmol m^{-2} d^{-1}	A	[1]
Flux FeOOH	F_{FeOOH}	variable	µmol m^{-2} d^{-1}	-	
Flux FeS	F_{FeS}	0	mmol m^{-2} d^{-1}	-	
Flux FeS_2	F_{FeS2}	0	mmol m^{-2} d^{-1}	-	
BIOGEOCHEMICAL PARAMETERS	**Symbol**	**Value**	**Units**	**Method**	**References**
Mixing depth	z_L	variable	cm	-	
Biodiffusion coefficient	$D_{b,0}$	variable	cm^2 yr^{-1}	-	
Bio-irrigation coefficient	α_0	variable	yr^{-1}	-	
Mineralisation constants	$k_{min,1}$	10^{-10}	yr^{-1}	A	[5]
	$k_{min,2}$	$3.16\ 10^{-10}$	yr^{-1}	A	[5]
	$k_{min,3}$	$3.16\ 10^{-9}$	yr^{-1}	A	[5]
	$k_{min,4}$	$3.16\ 10^{-8}$	yr^{-1}	A	[5]
	$k_{min,5}$	$3.16\ 10^{-7}$	yr^{-1}	A	[5]
	$k_{min,6}$	$3.16\ 10^{-6}$	yr^{-1}	A	[5]
	$k_{min,7}$	$3.16\ 10^{-5}$	yr^{-1}	A	[5]

	$k_{\min,8}$	$3.16\ 10^{-4}$	yr^{-1}	A	[5]
	$k_{\min,9}$	$3.16\ 10^{-3}$	yr^{-1}	A	[5]
	$k_{\min,10}$	$3.16\ 10^{-2}$	yr^{-1}	A	[5]
	$k_{\min,11}$	$3.16\ 10^{-1}$	yr^{-1}	A	[5]
	$k_{\min,12}$	3.16	yr^{-1}	A	[5]
	$k_{\min,13}$	31.6	yr^{-1}	A	[5]
	$k_{\min,14}$	100	yr^{-1}	A	[5]
	k_{H_2}	1000	yr^{-1}	A	[5]
N-to-C ratio organic matter	r_{CN}	16/106	-	-	-
Oxygen saturation constant	K_{O_2}	0.001	$mol\ m^{-3}$	A	[1]
Nitrate saturation constant	$K_{NO_3^-}$	0.010	$mol\ m^{-3}$	A	[3]
Nitrite saturation constant	$K_{NO_2^-}$	0.010	$mol\ m^{-3}$	A	[3]
MnO_2 saturation constant	K_{MnO_2}	20.8	$mol\ m^{-3}$	A	[1]
FeOOH saturation constant	K_{FeOOH}	260	$mol\ m^{-3}$	A	[1]
Sulphate saturation constant	$K_{SO_4^{2-}}$	0.5	$mol\ m^{-3}$	A	[1]
Nitrification	$k_{NIT.1}$	10^{+4}	$\mu mol^{-1}\ cm^3\ yr^{-1}$	A	[3]
Nitrification	$k_{NIT.2}$	10^{+4}	$\mu mol^{-1}\ cm^3\ yr^{-1}$	A	[3]
Manganese oxidation	k_{MnO}	$5\ 10^{+3}$	$\mu mol^{-1}\ cm^3\ yr^{-1}$	A	[4]
Ferrous iron oxidation	k_{FIO}	$5\ 10^{+5}$	$\mu mol^{-1}\ cm^3\ yr^{-1}$	A	[1]
Canonical sulphur oxidation	k_{CSO}	10^{+2}	$\mu mol^{-1}\ cm^3\ yr^{-1}$	A	[1]
Aerobic methane oxidation	k_{AMO}	10^{+2}	$\mu mol^{-1}\ cm^3\ yr^{-1}$	A	[1]
Iron sulphide oxidation	k_{ISO}	10^{+2}	$\mu mol^{-1}\ cm^3\ yr^{-1}$	A	[1]
Pyrite oxidation	k_{PyO}	1	$\mu mol^{-1}\ cm^3\ yr^{-1}$	A	[1]
Anamox	k_{ANA}	10^{+5}	$\mu mol^{-1}\ cm^3\ yr^{-1}$	A	[3]
Iron-mediated nitrate reduction	k_{NFO}	10^{+2}	$\mu mol^{-1}\ cm^3 yr^{-1}$	A	[3]
Sulphide-mediated nitrate reduction	k_{NSO}	0	$\mu mol^{-1}\ cm^3\ yr^{-1}$	A	[1]
Iron-mediated manganese reduction	$k_{MFO,HR}$	10^{+4}	$\mu mol^{-1}\ cm^3\ yr^{-1}$	A	[1]
Iron-mediated manganese reduction	$k_{MFO,MR}$	10^{+2}	$\mu mol^{-1}\ cm^3\ yr^{-1}$	A	[1]
Sulphide-mediated manganese reduction	$k_{MSO,HR}$	10^{+2}	$\mu mol^{-1}\ cm^3\ yr^{-1}$	A	[1]
Sulphide-mediated manganese reduction	$k_{MSO,MR}$	1	$\mu mol^{-1}\ cm^3\ yr^{-1}$	A	[1]
Sulphide-mediated iron reduction	$k_{SMI,HR}$	3	$\mu mol^{-1/2}\ cm^{3/2}\ yr^{-1}$	A	[5]
Sulphide-mediated iron reduction	$k_{SMI,MR}$	$3\ 10^{-3}$	$\mu mol^{-1/2}\ cm^{3/2}\ yr^{-1}$	A	[5]
Sulphide-mediated iron reduction	$k_{SMI,PR}$	$1\ 10^{-5}$	$\mu mol^{-1/2}\ cm^{3/2}\ yr^{-1}$	A	[5]
Sulphide-mediated iron reduction	$k_{SMI,U}$	0	$\mu mol^{-1/2}\ cm^{3/2}\ yr^{-1}$	A	[5]

Anaerobic methane oxidation	k_{AnMO}	10^{+2}	µmol^{-1} cm^3 yr^{-1}	A	[1]
Kinetic constant ammonium sorption	k_{AmS}	10^{-4}	µmol cm^3 yr^{-1}	A	[3]
Equilibrium constant ammonium sorption	$K_{ads}^{NH_4^+}$	4.16	-	A	[3]
Equilibrium constant ferrous iron sorption	$K_{ads}^{Fe^{2+}}$	0	-	A	[1]
Elemental sulphur disproportionation	k_{SDP}	1	yr^{-1}	A	[1]
Iron sulphide precipitation	k_{ISP}	10^{+3}	µmol cm^3 yr^{-1}	A	[1]
Iron sulphide dissolution	k_{ISD}	3	yr^{-1}	A	[6]
Kinetic exponent iron sulphide dissolution	n_{ISD}	1	-	A	[6]
Pyrite precipitation	$k_{PyP.1}$	3.25	µmol^{-1} cm^3 yr^{-1}	C	[7],[8]
Pyrite precipitation	$k_{PyP.2}$	3.25	µmol^{-1} cm^3 yr^{-1}	C	[7],[8]
Manganese oxide ageing	k_{MOA}	1.7	yr^{-1}	C	[1],[9]
Iron oxide ageing	k_{IOA}	0.6	yr^{-1}	C	[1],[9]

[1] Flux value for the standard model of Dale et al. (2015), this value is equally distributed among the HR and MR fractions.

Table S6: List of fixed parameters included in the model. Solid-phase concentrations are expressed per unit volume of solid phase. "Method" refers to the procedure by which parameter values are constrained: A = Literature values, B = model calibration. Note that all isotope values are given relative to the IRMM-14 standard. Variable parameters indicate parameters that are changed during the sensitivity experiments. Please refer to the main text for these parameters.

References: [1] Dale et al. (2015), [2] Dauphas et al. (2017), [3] Bohlen et al. (2011), [4] Van Cappellen and Wang (1995), [5] Poulton and Canfield, (2005), [6] van de Velde and Meysman (2016), [7] van de Velde et al. (2020), [8] Rickard (2002), [9] Berg et al. (2003).